RESEARCH ARTICLE

MEDICAL PHYSICS

Simultaneous temperature and viscosity estimation capability via magnetic nanoparticle relaxation

Mustafa Utkur[1,2] | Emine Ulku Saritas[1,2,3]

[1] Department of Electrical and Electronics Engineering, Bilkent University, Ankara, Turkey

[2] National Magnetic Resonance Research Center (UMRAM), Bilkent University, Ankara, Turkey

[3] Neuroscience Program, Aysel Sabuncu Brain Research Center, Bilkent University, Ankara, Turkey

Correspondence
Mustafa Utkur, Department of Electrical and Electronics Engineering, Bilkent University, Ankara 06800, Turkey; Emine Ulku Saritas, Department of Electrical and Electronics Engineering, Bilkent University, Ankara 06800, Turkey.
Email: mustafa.utkur@bilkent.edu.tr; saritas@ee.bilkent.edu.tr

Abstract

Purpose: Magnetic particle imaging (MPI) is emerging as a highly promising imaging modality. Magnetic nanoparticles (MNPs) are used as imaging tracers in MPI, and their relaxation behavior provides the foundation for its functional imaging capability. Since MNPs are also utilized in magnetic fluid hyperthermia (MFH) and MPI enables localized MFH, temperature mapping arises as an important application area of MPI. To achieve accurate temperature estimations, however, one must also take into account the confounding effects of viscosity on the MPI signal. In this work, we analyze the effects of temperature and viscosity on MNP relaxation and determine temperature and viscosity sensitivities of relaxation time constant estimations via TAURUS (TAU estimation via Recovery of Underlying mirror Symmetry) at a wide range of operating points to empower simultaneous mapping of these two parameters.

Methods: A total of 15 samples were prepared to reach four target viscosity levels (0.9–3.6 mPa·s) at five different temperatures (25–45°C). Experiments were performed on a magnetic particle spectrometer (MPS) setup at 60 different operating points at drive field amplitudes ranging between 5 and 25 mT and frequencies ranging between 1 and 7 kHz. To enable these extensive experiments, an in-house arbitrary-waveform MPS setup with temperature-controlled heating capability was developed. The operating points were divided into four groups with comparable signal levels to maximize signal gain during rapid signal acquisition. The relaxation time constants were estimated via TAURUS, by restoring the underlying mirror symmetry property of the positive and negative half cycles of the time-domain MNP response. The relative time constants with respect to the drive field period, $\hat{\tau}$, were computed to enable quantitative comparison across different operating points. At each operating point, a linear fit was performed to $\hat{\tau}$ as a function of each functional parameter (i.e., temperature or viscosity). The slopes of these linear fits were utilized to compute the temperature and viscosity sensitivities of TAURUS.

Results: Except for outlier behaviors at 1 kHz, the following global trends were observed: $\hat{\tau}$ decreases with drive field amplitude, increases with drive field frequency, decreases with temperature, and increases with viscosity. The temperature sensitivity varies slowly across the operating points and reaches a maximum value of 1.18%/°C. In contrast, viscosity sensitivity is high at low frequencies around 1 kHz with a maximum value of 13.4%/(mPa·s) but rapidly falls after 3 kHz. These results suggest that the simultaneous estimation of temperature and viscosity can be achieved by performing measurements at two different drive field settings that provide complementary temperature/viscosity sensitivities. Alternatively, temperature estimation alone can be achieved with a single measurement at drive field frequencies above 3 kHz, where viscosity sensitivity is minimized.

Conclusions: This work demonstrates highly promising temperature and viscosity sensitivities for TAURUS, highlighting its potential for simultaneous estimation of these two environmental parameters via MNP relaxation. The findings of this work reveal the potential of a hybrid MPI–MFH system for real-time monitored and localized thermal ablation treatment of cancer.

1 | INTRODUCTION

Magnetic particle imaging (MPI) is a tomographic imaging modality,[1] where magnetic nanoparticles (MNPs) are used as imaging tracers. These MNPs are typically cleared by the liver and hence are kidney-safe. Furthermore, the magnetic fields used in MPI are nonionizing, as their frequencies are in the low kHz range.[2] MPI exploits the nonlinear magnetization characteristics of MNPs by applying an AC magnetic field (i.e., the drive field) to generate a signal response, from which an MPI image of the underlying MNP distribution is reconstructed without any background signal from the tissue. In reality, due to the relaxation effects, the magnetic moments of MNPs cannot align with the drive field instantaneously, and this delayed response causes a loss of signal-to-noise ratio (SNR) and a blurring of the MPI image. Although the relaxation behavior can deteriorate image quality, it also provides functional imaging capability to MPI for applications such as temperature mapping,[3–5] viscosity mapping,[6–9] and identifying inflammation.[10,11] While the theoretical aspects of relaxation mechanisms under AC fields need further investigation, their effects on the MPI signal have been studied via experimental procedures.

Temperature mapping, or thermometry, presents itself as one of the important application areas of MPI, especially considering the fact that MNPs are also used in thermal therapy applications such as magnetic fluid hyperthermia (MFH). When subjected to relatively high-frequency AC magnetic fields (e.g., 300–400 kHz), MNPs become very efficient heat sources that can be used to target and heat up tumor tissue without any depth limitations and achieve immunogenicity.[12–14] The heat generation property of MNPs is based on the same relaxation mechanisms that give MPI its functional imaging capability. Moreover, the hardware of MPI and MFH is compatible, enabling hybrid MPI-MFH systems to be constructed for image-guided localized heat therapy.[15–17] By positioning the field free region of an MPI scanner over the tumor region, MPI can equip MFH with localized heating capability.[18,19] In addition, the MPI image can be utilized to predict the temperature rise prior to MFH therapy[18,20,21] or to provide real-time temperature feedback through temperature mapping during MFH therapy (e.g., via a short break of imaging).

The current thermal ablation studies for prostate and breast cancers utilize integrated magnetic resonance imaging (MRI) and high-intensity focused ultrasound (HIFU) systems, where MRI noninvasively monitors the temperature and HIFU delivers thermal energy to the tumor tissue.[22,23] Some of the major drawbacks of this approach include extremely long treatment times reaching up to hours and technical limitations in HIFU beam conformation that may result in inhomogeneous thermal dose or damage to the surrounding healthy tissue.[24] Here, a hybrid MPI–MFH system emerges as a very promising alternative for thermal ablation treatment of cancer, as MFH is depth independent and the imaging duration of MPI is in the range of seconds to minutes.

To date, several groups have proposed different methods to estimate temperature in MPI. Some studies worked with the spectral information of the MNP response using a magnetic particle spectrometer (MPS) setup, where the ratios of harmonics were related to the temperature change.[3,17,25–27] Other studies in an MPI scanner utilized a system function approach, where the frequency response of MNPs at different temperatures was acquired during a calibration procedure, and the temperatures during imaging were mapped by solving a linear system of equations.[4,28,29] In contrast to the aforementioned spectral methods, we have previously proposed a relaxation mapping technique called TAURUS (TAU estimation via Recovery of Underlying mirror Symmetry), in which the time-domain MNP response is utilized to estimate a relaxation time constant that recovers the underlying mirror-symmetric response.[6] A powerful feature of this technique is that it can be directly applied to both MPS and MPI signal responses since the underlying mirror symmetry assumption is valid independent of the spatial distribution of MNPs.[9,30] We have previously demonstrated the viscosity mapping capability of TAURUS on our in-house MPI scanner and obtained the optimal drive field parameters using commercially available multicore MNPs.[9]

An important consideration for temperature estimation is that the viscosity of the environment also needs to be accounted for, as these two parameters are bound to have confounding effects on the MNP signal.[31] Different tissues may show varying degrees of change in their viscosity levels as a function of temperature,[32]

or different initial viscosity levels may lead to different trends on the relaxation time constant as a function of temperature. These factors can in turn lead to erroneous temperature estimations. Therefore, to achieve accurate temperature estimations, either the MNP signal needs to be desensitized to the viscosity effect, or viscosity and temperature need to be estimated simultaneously. In this work, we experimentally analyze the effects of temperature on TAURUS while taking the viscosity level into account to highlight its potential for simultaneous estimation of these two parameters. With extensive experiments, we cover the therapeutically applicable temperature range (25–45°C) and the biologically relevant viscosity range (<4 mPa·s) and utilize 60 different operating points with drive field amplitudes ranging between 5 and 25 mT and frequencies ranging between 1 and 7 kHz. To enable this experimental procedure, we have developed an in-house arbitrary-waveform MPS setup with temperature-controlled heating capability, which can rapidly acquire a wide range of operating points grouped together with respect to their signal levels to ensure gain maximization. The results show that the temperature sensitivity of TAURUS slowly varies in these drive field settings and reaches a maximum value of 1.18%/°C, whereas viscosity sensitivity is high at lower frequencies around 1 kHz with a maximum value of 13.4%/(mPa·s). Furthermore, we propose strategies for simultaneous estimation of temperature and viscosity using two different drive field settings, or temperature estimation alone at frequencies where viscosity sensitivity is minimized.

2 | THEORY

Using Faraday's law of induction, the received signal in MPI can be expressed as follows[33,34]:

$$
\begin{aligned}
s_{\text{received}}(t) &= -\frac{d\phi(t)}{dt} \\
&= -\mu_0 \int_V \mathbf{B_1}(\mathbf{r}) \cdot \frac{\partial \mathbf{M}(\mathbf{r}, t)}{\partial t} \, dV \\
&= -\mu_0 \int_V \mathbf{B_1}(\mathbf{r}) \cdot c(\mathbf{r}) \frac{\partial \bar{m}(H(\mathbf{r}, t))}{\partial t} \, dV
\end{aligned}
\quad (1)
$$

Here, $\phi(t)$ is the magnetic flux, $\mathbf{B_1}(\mathbf{r})$ is the position-dependent receive coil sensitivity, $\mathbf{H}(\mathbf{r}, t)$ is the applied field, and "·" indicates vector dot product. In addition, $\mathbf{M}(\mathbf{r}, t)$ is the MNP magnetization, which is equal to the multiplication of MNP concentration, $c(\mathbf{r})$, and the average magnetic dipole moment, $\bar{m}(H)$.

In the case of a typical MPS setup, we can assume that the applied field over the sample is homogeneous in space and unidirectional (e.g., only along the z-direction), the receive coil sensitivity in that direction is

also homogeneous, and the MNP concentration is uniform within the sample. Under these assumptions, Equation (1) can be rewritten as

$$
\begin{aligned}
s_{\text{received}}(t) &= -\mu_0 \int_V B_1 c \frac{d\bar{m}(H(t))}{dt} \, dV \\
&= -\mu_0 B_1 c V_S \frac{d\bar{m}(H(t))}{dt}
\end{aligned}
\quad (2)
$$

Here, V_S is the sample volume and the multiplication of c and V_S is equal to the total iron mass within the sample.

Assuming that the MNPs follow Langevin physics with an adiabatic approximation that their dipole moments immediately align with the applied field, $s_{\text{adiabatic}}(t)$ can be written as

$$
\begin{aligned}
s_{\text{adiabatic}}(t) &= -\mu_0 B_1 c V_S m \frac{d\mathcal{L}(kH(t))}{dt}, \\
&= -\alpha \dot{\mathcal{L}}(kH(t)) \dot{H}(t)
\end{aligned}
\quad (3)
$$

where

$$
\alpha = \mu_0 B_1 c V_S m k. \quad (4)
$$

Here, m is the magnetic moment of a single MNP, $\mathcal{L}(\cdot)$ is the Langevin function and $\dot{\mathcal{L}}(\cdot)$ is its derivative, and k is a parameter that depends on m and MNP temperature.

In reality, the adiabatic approximation is not valid for rapidly time-varying applied fields, where the alignment of the magnetic moment lags behind due to the relaxation mechanism of MNPs through a combination of an external physical rotation (i.e., Brownian relaxation) and an internal rotation (i.e., Néel relaxation).[35,36] The governing relations for these two relaxation mechanisms for the "zero-field" case (i.e., when a DC field is abruptly set to zero) are given as follows:

$$
\tau_B = \frac{3\eta V_h}{k_B T}, \quad (5)
$$

$$
\tau_N = \tau_0 \left(\frac{\sqrt{\pi}}{2} \right) \left(\sqrt{\frac{k_B T}{K V_c}} \right) e^{\frac{K V_c}{k_B T}}. \quad (6)
$$

Here, τ_B is the Brownian relaxation time constant, η is the viscosity of the medium, V_h is the hydrodynamic volume of the MNP, k_B is the Boltzmann's constant, and T is the temperature. In addition, τ_N is the Néel relaxation time constant, τ_0 is the so-called attempt time (in the order of ~1 ns),[7,37] and V_c and K are the core volume and the anisotropy constant of the MNP, respectively.

As seen in Equations (5) and (6), the relaxation time constants are dependent on the environmental conditions, namely temperature and viscosity. This feature

makes the relaxation mechanism particularly important for functional imaging purposes in MPI. However, the zero-field condition does not directly apply in MPI, since a continuous sinusoidal drive field is utilized together with simultaneous signal reception. While the theoretical aspect of the relaxation mechanisms under an oscillating magnetic field is still incomplete,[38] the "effective" relaxation process in the case of a sinusoidal drive field was previously modeled as a first-order Debye process, where the relaxation behavior causes the time-domain MNP response to simultaneously get delayed in time and lose signal amplitude.[39,40] Accordingly, the relationship between $s_{received}(t)$ and $s_{adiabatic}(t)$ is expressed as follows:

$$s_{received}(t) = s_{adiabatic}(t) * \left\{ \frac{1}{\tau} e^{-\frac{t}{\tau}} u(t) \right\}. \quad (7)$$

Here, $u(t)$ is the Heaviside step function and "$*$" denotes convolution in the time domain. In this phenomenological model, τ denotes the effective relaxation time constant.

As described in our previous work, $s_{adiabatic}(t)$ has mirror symmetric positive and negative half cycles, but that mirror symmetry is broken due to the relaxation effects on $s_{received}(t)$. We have previously developed a technique called TAURUS, which directly estimates τ as follows[6,9,30]:

$$\tau = \frac{S_{pos}^*(f) + S_{neg}(f)}{i2\pi f(S_{pos}^*(f) - S_{neg}(f))}. \quad (8)$$

Here, $S_{pos}(f)$ and $S_{neg}(f)$ are the Fourier transforms of the positive and negative half cycles of $s_{received}(t)$, respectively, and the superscript "$*$" sign denotes complex conjugation.

Note that the relaxation time constant, τ, in Equations (7) and (8) is also dependent on both temperature and viscosity,[6] since τ corresponds to an effective combination of τ_B and τ_N under a sinusoidal drive field. Furthermore, viscosity is known to decrease with temperature, which causes these two environmental parameters to have confounding effects on the MNP response.[31] In the following sections, the effects of temperature and viscosity on τ are analyzed under a wide range of drive field settings using an in-house arbitrary-waveform MPS setup.

3 | MATERIALS AND METHODS

3.1 | Sample preparation

A total of 15 samples with glycerol mass percentages ranging between 0.4% and 56.3% were prepared to achieve targeted biologically relevant viscosity levels at different temperatures, following the formulations in
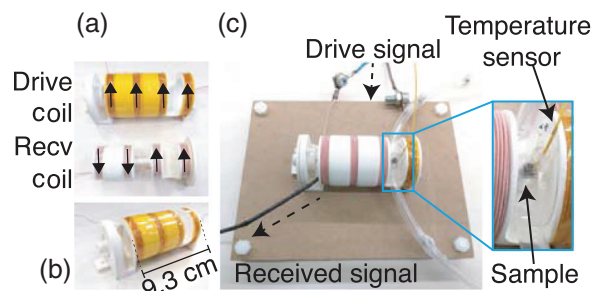

FIGURE 1 In-house arbitrary-waveform MPS setup, designed to enable temperature-controlled heating of the MNP samples. (a) The drive coil consisted of four sections and the receive coil was a two-section gradiometer-type coil that mirrors the structure of the drive coil. The arrows show the winding directions. (b) The drive and receive coils were placed coaxially, and the moving subparts of the receive coil were adjusted with a screw mechanism to minimize the mutual inductance between the two coils. (c) An overview of the experimental setup. The samples were placed in a temperature-controlled water tube, and the temperature of each sample was monitored with a fiber optic temperature probe. The dashed arrows indicate the direction of signal flow

Ref. 41. The samples were prepared at a room temperature of 25°C in 0.2 mL PCR tubes. The corresponding glycerol volume percentages at 25°C ranged between 0.3% and 50.5%, which were calculated based on the densities of glycerol and water at 25°C.[42,43] At 25°C, each sample had a total volume of 150 μL and contained 60 μL of undiluted Perimag nanoparticles (Micromod GmbH, Germany) at 303.6 mM initial concentration (i.e., each sample had 1 mg Fe). For the remaining 90 μL, varying volumes of double-distilled water and glycerol were added. The viscosity levels at different temperatures were calculated based on the mass percentages, as described by Ref. 41. We assumed that undiluted Perimag has the same viscosity as distilled water in the calculations. As seen in Table 1, at fixed temperature, viscosity increases with increasing glycerol percentage. On the other hand, the viscosity of a sample at a fixed glycerol percentage decreases with increasing temperature. This physical phenomenon enabled us to design experiments such that four different target viscosity levels (0.9, 1.8, 2.7, and 3.6 mPa·s) were achieved at five different temperatures (25, 30, 35, 40, and 45°C), as highlighted with bold font in Table 1.

3.2 | Experimental setup and procedures

Experiments were performed on our in-house arbitrary-waveform MPS setup (see Figure 1). The nanoparticle samples were placed in a temperature-controlled water tube during the experiments. To accommodate the placement of this structure into the measurement chamber (see Figure 1c), a 41.5-mm inner diameter drive coil was designed to consist of four sections of

TABLE 1 Glycerol percentages and viscosity levels at five different temperatures for the 15 MNP samples used in this work. Each sample contained 60 µL of undiluted Perimag nanoparticles at 25°C. The bold values highlight four different target viscosity levels achieved at five different temperatures

Glycerol % volume at 25°C	Glycerol % weight	Viscosity (mPa·s)				
		25°C	30°C	35°C	40°C	45°C
0.3	0.4	**0.90**	0.81	0.73	0.66	0.60
4.1	5.1	1.01	**0.90**	0.81	0.74	0.67
7.6	9.4	1.13	1.00	**0.90**	0.81	0.74
11.0	13.5	1.26	1.12	1.00	**0.90**	0.82
14.2	17.3	1.40	1.24	1.11	1.00	**0.90**
21.1	25.2	**1.80**	1.58	1.40	1.25	1.12
24.6	29.2	2.06	**1.80**	1.59	1.41	1.27
28.0	32.9	2.36	2.06	**1.81**	1.60	1.43
31.2	36.4	**2.71**	2.34	2.05	**1.80**	1.60
34.5	39.9	3.13	**2.69**	2.34	2.05	**1.82**
37.7	43.3	**3.63**	3.10	**2.68**	2.34	2.06
41.0	46.7	4.25	**3.61**	3.11	**2.70**	2.36
44.2	50.0	5.00	4.22	**3.61**	3.11	**2.71**
47.4	53.2	5.93	4.97	4.22	**3.61**	3.13
50.5	56.3	7.06	5.87	4.94	4.21	**3.62**

equal length separated by 20-mm gaps (see Figure 1a). Each section had three layers of windings with six turns per layer, wound using 125-strand 40 AWG Litz wire (MWS Wire Industries). The sensitivity of the drive coil was measured using a gaussmeter (LakeShore, 475 DSP) by applying 1 A of current at frequencies ranging between 1 and 10 kHz. The sensitivity was measured as 0.65 mT/A, with a negligible standard deviation of 2 µT/A in this frequency range.

As shown in Figure 1a, an 11-mm inner diameter receive coil was designed as a two-section gradiometer-type coil, where each section was further divided into two subparts to mirror the structure of the drive coil. These subparts were separated by 21.6-mm gaps, and each part contained 15 layers with nine turns per layer, wound using 125-strand 44 AWG Litz wire (MWS Wire Industries). The two subparts where the sample was placed in between were fixed to the drive coil, whereas the other two subparts were attached to a plastic screw to enable fine-tuned adjustment of their position. These moving subparts enabled high precision decoupling between the drive and the receive coils, which were placed coaxially as shown in Figure 1b. The sensitivity of the receive coil was measured as 4.1 mT/A at 1 kHz, and its self-resonance was measured to be above 200 kHz, which is well outside the range of frequencies of interest in this work.

The resistance and the inductance of the drive coil were measured with an LCR meter (GW Instek LCR-8100) as 0.29 Ω and 92 µH, respectively, for frequencies lower than 10 kHz. Owing to the low inductance of the drive coil, the need for impedance matching was eliminated so that the drive coil could be directly connected to an AC power amplifier (AE Techron 7224). This arbitrary-waveform MPS characteristic[44,45] enabled us to apply any drive field signal below 10 kHz without using additional capacitive circuitry.

The experimental setup was controlled with a fully automated custom script in MATLAB (Mathworks, Natick, MA, USA). The drive field waveform was sent to the AC power amplifier via a data acquisition card (NI PCI-6115), and the received signal was also digitized using the same card with a sampling rate of 2 MS/s. The PCR tubes that contained the samples were placed vertically in the holes cut out on a water tube and sealed with hot glue to prevent water leakages. A temperature-controlled water pump was used to circulate hot water inside the water tube, heating up the samples to the desired temperatures via conduction. During the experiments, the temperature of the sample of interest was monitored with a fiber optic temperature probe (Neoptix Reflex-4) placed inside the PCR tube. The drive coil was cooled with cold air to prevent resistive-heating-induced field fluctuations, and its temperature was monitored with a thermal camera (Seek Thermal Reveal Pro). On the receive side, the nanoparticle signal first passed through an analog Butterworth low pass filter (SRS SIM965) with 200 kHz cutoff frequency and 48 dB/octave roll-off, and then amplified with a BJT preamplifier (SRS SIM911).

The samples were tested at seven different drive field frequencies (f_d) ranging between 1 and 7 kHz with 1 kHz increments and nine different drive field amplitudes ranging between 5 and 25 mT with 2.5 mT
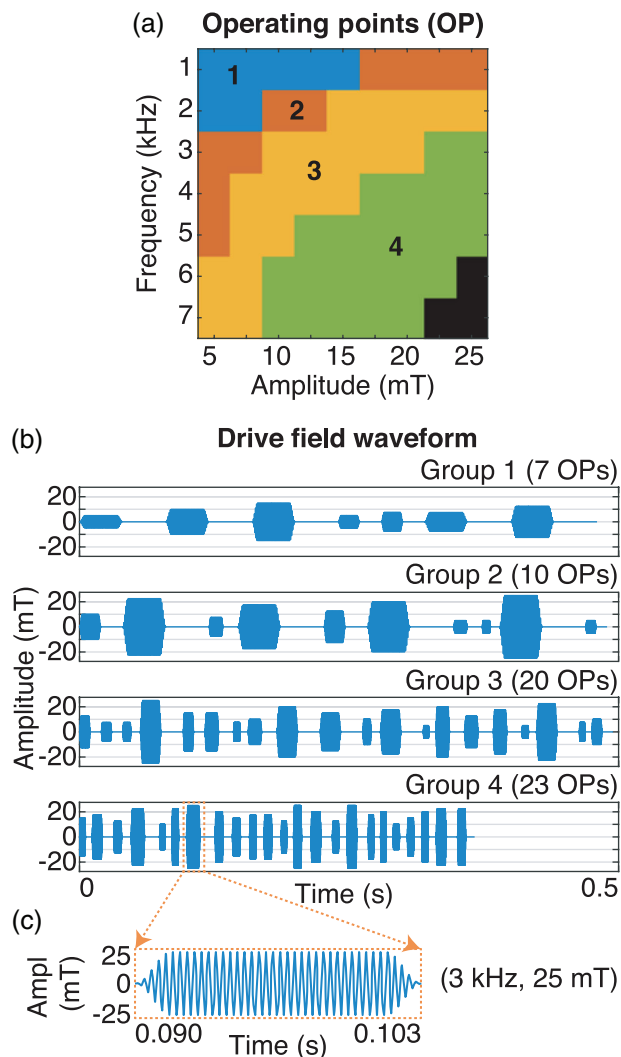
FIGURE 2 Operating points and the corresponding drive field waveforms. (a) 60 different operating points were divided into four groups with comparable signal amplitudes, as enumerated and marked with colors. The grouping ensured that the peak signal amplitude within each group varied by at most threefold, enabling maximization of the signal gain. The black portion indicates the operating points that exceeded the hardware limitations. (b) The drive field waveform for each group and the number of operating points in each group. The waveform at each operating point contained 40 periods followed by a gap of the same duration. (c) A zoom-in plot, showing an example drive field waveform at (3 kHz, 25 mT)

increments. Among the resulting 63 operating points, the following three operating points could not be utilized due to hardware limitations: (6 kHz, 25 mT), (7 kHz, 22.5 mT), (7 kHz, 25 mT). Since the received signal was picked up inductively, its amplitude is approximately proportional to both the drive field amplitude and frequency (see Equation 3). Therefore, the remaining 60 operating points were divided into four groups with comparable signal amplitudes, as shown in Figure 2a. Within each group, the peak signal amplitude varied by at most threefold among different operating points. The drive field waveform at each operating point contained 40

periods followed by a gap of the same duration (see Figure 2b). A calibration stage was performed prior to the measurement stage in which the drive amplitudes within a group were calibrated with a Rogowski current probe (LFR 06/6/300) using the coil sensitivity data measured earlier. Then, a single gain value for that group was selected as the maximum gain that does not overload the preamplifier. In the measurement stage, two consecutive acquisitions were performed: an empty-chamber baseline acquisition and an acquisition with the sample. In each case, the mean of four acquisitions was recorded to increase the SNR. Furthermore, all measurements were repeated three times by randomizing the ordering of the operating points within each group, with the goal of eliminating potential ordering-related biases in the results. Overall, a total of 3600 measurements were performed (i.e., four viscosity levels, five temperatures, 60 operating points, and three repetitions).

3.3 | Data postprocessing

All postprocessing was performed in MATLAB. Each baseline measurement was first subtracted from the corresponding sample measurement to eliminate any residual direct-feedthrough and potential interferences, and digitally upsampled to 16 MS/s sampling rate. Then, the MNP signal was divided by the corresponding preamplifier gain used for that measurement. Next, the noise level was calculated using the nonharmonic frequencies, and the harmonics with signal levels above the noise level were selected. To avoid interference at the self-resonance frequency of the receive coil, only the frequencies smaller than 200 kHz were utilized. After that, a high-order zero-phase digital low-pass filter was applied in the time domain, with the cutoff frequency set to the highest selected harmonic frequency.

3.4 | Time constant and sensitivity analysis

The relaxation time constant, τ, of the nanoparticle signal was estimated using TAURUS as described in Equation (8). The range of τ values among different drive field frequencies can differ considerably. Therefore, for quantitative comparison purposes, τ values were converted to percentages with respect to a single drive field period, $P_d = 1/f_d$, that is,

$$\hat{\tau} = \frac{\tau}{P_d} \times 100. \tag{9}$$

Here, $\hat{\tau}$ enables us to quantify the relative delay with respect to the period caused by relaxation.

Next, at each operating point, a linear fit was performed to the $\hat{\tau}$ values as a function of each functional parameter (i.e., temperature or viscosity) to quantify the sensitivity of the relaxation time constant to that parameter. The slope of this linear fit was utilized to define a sensitivity metric. Accordingly, the relative temperature sensitivity of an operating point can be expressed as follows:

$$T_{sensitivity} = \frac{|\hat{\tau}_{end} - \hat{\tau}_{start}|/\hat{\tau}_{start}}{T_{end} - T_{start}} \times 100$$

$$= \frac{|\tau_{end} - \tau_{start}|/\tau_{start}}{T_{end} - T_{start}} \times 100 \qquad (10)$$

Here, $T_{sensitivity}$ describes the percentage change in $\hat{\tau}$ (or τ) per 1°C change in temperature and has the unit of %/°C. For the experiments in this work, $T_{start} = 25°C$ and $T_{end} = 45°C$, and $\hat{\tau}_{start}$ and $\hat{\tau}_{end}$ are the $\hat{\tau}$ values corresponding to those temperatures on the fitted line. Likewise, relative viscosity sensitivity of an operating point can be expressed as follows:

$$\eta_{sensitivity} = \frac{|\hat{\tau}_{end} - \hat{\tau}_{start}|/\hat{\tau}_{start}}{\eta_{end} - \eta_{start}} \times 100$$

$$= \frac{|\tau_{end} - \tau_{start}|/\tau_{start}}{\eta_{end} - \eta_{start}} \times 100 \qquad (11)$$

Here, $\eta_{sensitivity}$ describes the percentage change in $\hat{\tau}$ (or τ) per 1 mPa·s change in viscosity and has the unit of %/(mPa·s). For the experiments performed in this work, $\eta_{start} = 0.9$ mPa·s and $\eta_{end} = 3.6$ mPa·s, and $\hat{\tau}_{start}$ and $\hat{\tau}_{end}$ are the $\hat{\tau}$ values corresponding to those viscosity levels on the fitted line.

4 | RESULTS

4.1 | Time constant versus operating point

The relative time constants with respect to period, $\hat{\tau}$'s, computed using Equation (9) are plotted in Figure 3 as a function of the drive field amplitude at seven different frequencies. The error bars indicate standard deviations (STD) across three repetitions. Here, the rows and the columns correspond to the results at distinct viscosity levels and temperatures, respectively. Apart from a few exceptional cases at low drive field amplitudes, $\hat{\tau}$ decreases with drive field amplitude at all frequencies, as the MNPs align faster under larger forcing fields. In contrast, $\hat{\tau}$ increases with drive field frequency, as the delay in the alignment of the MNPs becomes more substantial at shorter periods. Interestingly, there is an outlier behavior at 0.9 mPa·s where $\hat{\tau}$ reaches its highest values at the lowest frequency of 1 kHz. In general, comparing the amount of change in $\hat{\tau}$ as the amplitude is
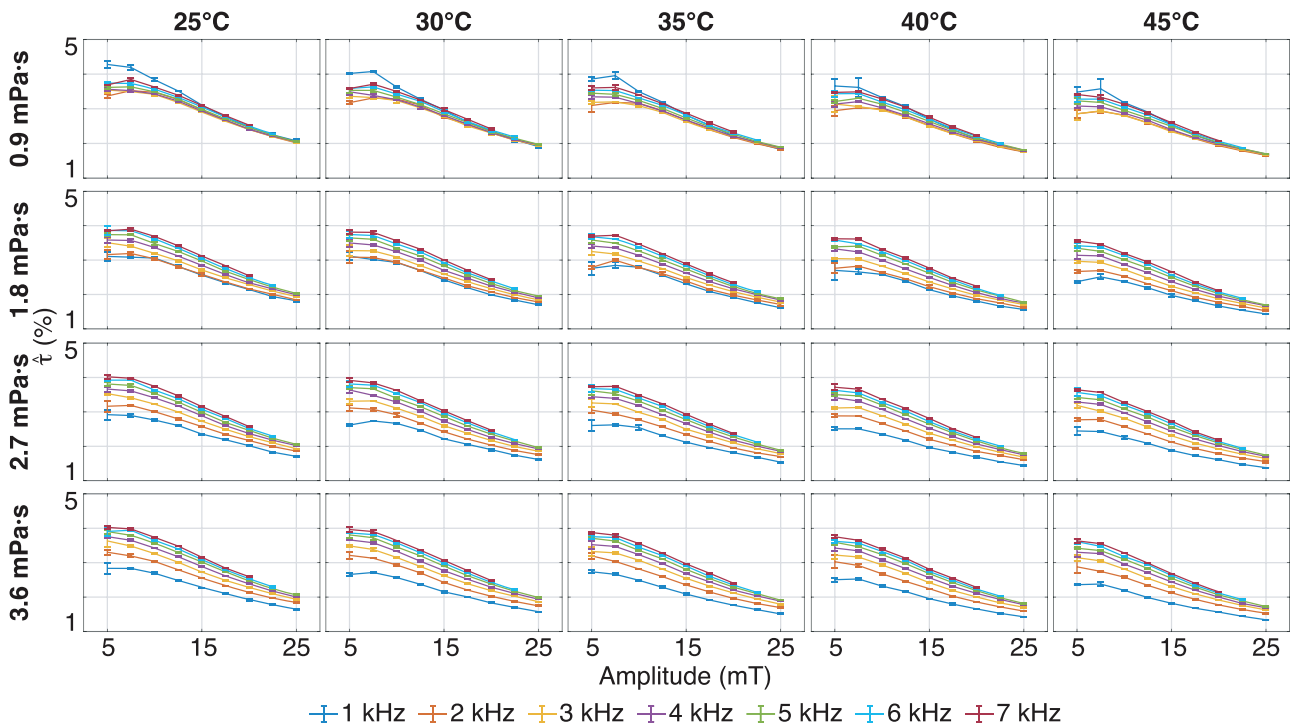

FIGURE 3 The relative time constants with respect to the drive field period, $\hat{\tau}$'s, plotted as a function of the drive field amplitude at seven different frequencies. The rows and the columns correspond to distinct viscosity levels and temperatures, respectively. Overall, $\hat{\tau}$ decreases with drive field amplitude and increases with drive field frequency. Here, the error bars denote standard deviations across three repetitions
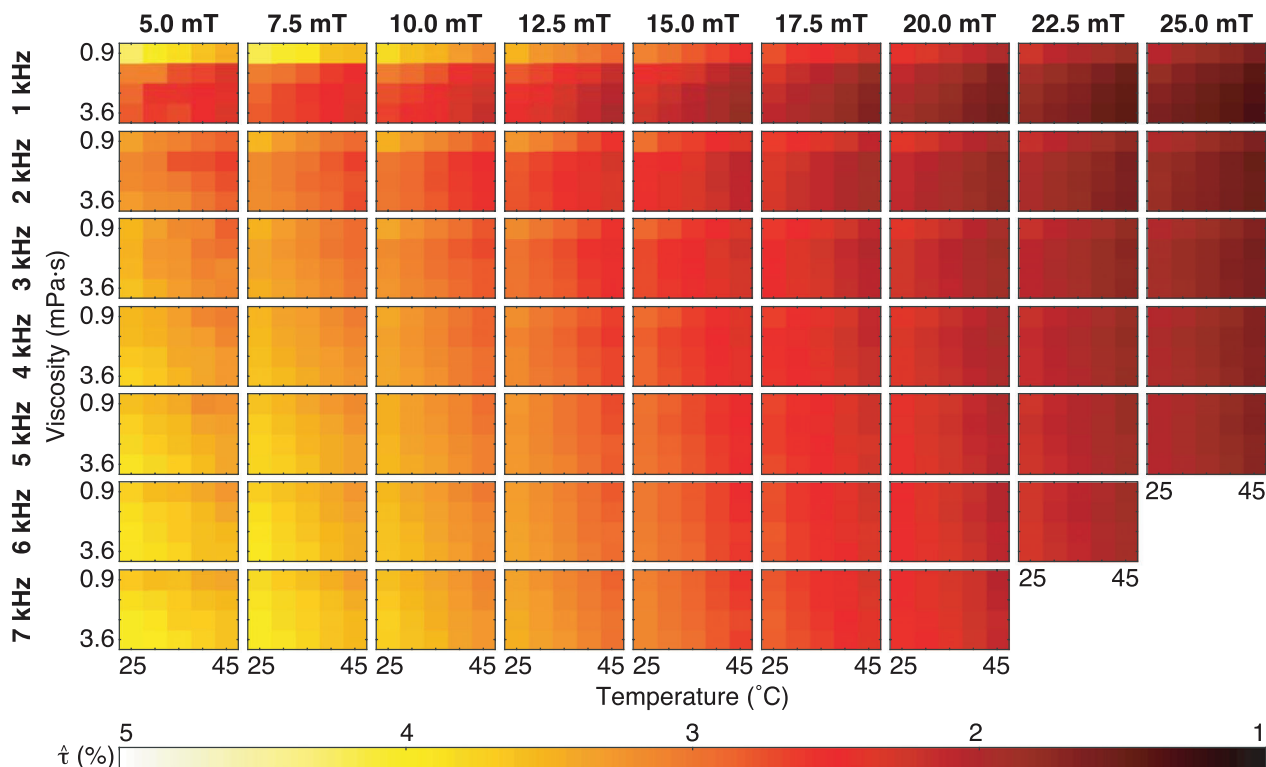
FIGURE 4   The mean values of $\hat{\tau}$ at 60 different operating points displayed as color maps, as a function of viscosity and temperature. The rows and the columns correspond to the results at distinct drive field frequencies and amplitudes, respectively. Overall, $\hat{\tau}$ decreases with temperature and increases with viscosity

increased fivefold and the frequency is increased sevenfold, it can be observed that the effect of amplitude on $\hat{\tau}$ is more dramatic than that of frequency. As the field is increased from 5 to 25 mT, $\hat{\tau}$ decreases by 45% on average (from 3.25% ± 0.38% to 1.78% ± 0.17%, mean ± STD). On the other hand, as the frequency is increased from 1 to 7 kHz, $\hat{\tau}$ increases by 24% on average (from 2.53% ± 0.58% to 3.14% ± 0.53%, mean ± STD).

In Figure 4, the mean values of $\hat{\tau}$ at 60 different operating points are displayed as color maps, where the rows and the columns correspond to the results at distinct drive field frequencies and amplitudes, respectively. As stated previously, $\hat{\tau}$ decreases towards the low-frequency high-amplitude operating points, reaching the lowest values around (1 kHz, 25 mT) and the highest values around (7 kHz, 5 mT). The outlier behavior at 1 kHz and at 0.9 mPa·s in Figure 3 is also clearly visible in Figure 4 where $\hat{\tau}$ shows an abrupt increase. This behavior persists at higher temperatures but diminishes at higher viscosity levels. As expected from Equations (5) and (6), there is a global decrease in $\hat{\tau}$ as temperature increases. Moreover, $\hat{\tau}$ increases as viscosity increases at high frequencies, as expected from Equation (5). However, this trend changes at low frequencies indicating the insufficiency of the zero-field relaxation theory in explaining the trends for sinusoidal drive fields.

4.2 | Temperature and viscosity sensitivities

In Figure 5, $\hat{\tau}$ is plotted with respect to each functional parameter (i.e., temperature or viscosity) at four selected operating points: (1 kHz, 5 mT), (1 kHz, 25 mT), (7 kHz, 5 mT), and (6 kHz, 22.5 mT). In Figure 5a, a line is fitted to each $\hat{\tau}$ versus temperature curve at four different viscosity levels. Likewise, in Figure 5(b), a line is fitted to each $\hat{\tau}$ versus viscosity curve at five different temperatures. Here, the sensitivity metrics given in Equations (10) and (11) are computed using the slopes of the above-mentioned linear fits, and they describe the percentage change in $\hat{\tau}$ as a function of temperature or viscosity. Accordingly, in Figure 5a, $\hat{\tau}$ decreases with temperature at all operating points and at all viscosity levels, displaying the highest temperature sensitivities at 1 kHz. For example, at (1 kHz, 5 mT), the temperature sensitivity is 0.93 %/°C at 0.9 mPa·s. As the frequency increases, the temperature sensitivity decreases, reaching a value of 0.36 %/°C at (7 kHz, 5 mT) at 0.9 mPa·s. In Figure 5b, $\hat{\tau}$ decreases rapidly with increasing viscosity at all temperatures at (1 kHz, 5 mT), corresponding to a viscosity sensitivity of 12.7%/(mPa·s) at 25°C. In contrast, $\hat{\tau}$ versus viscosity curves flatten out at higher frequencies, indicating reduced sensitivities to viscosity. For example, at (6 kHz, 22.5 mT), the viscosity sensitivity is
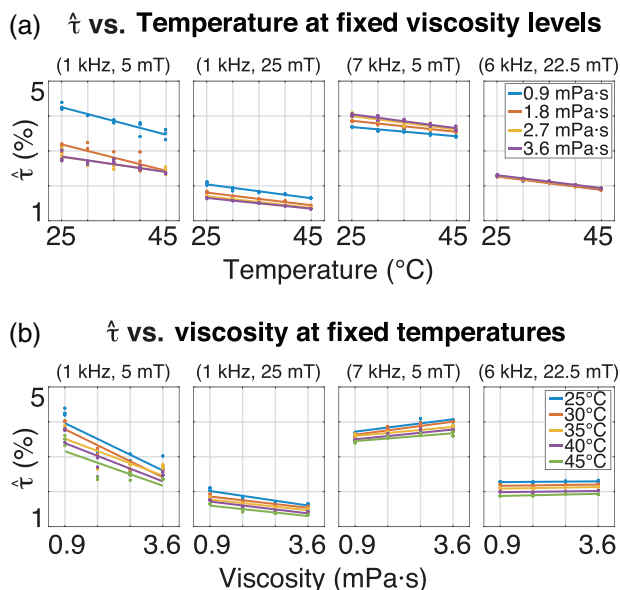
(a) $\hat{\tau}$ **vs. Temperature at fixed viscosity levels**

(b) $\hat{\tau}$ **vs. viscosity at fixed temperatures**

FIGURE 5 $\hat{\tau}$ with respect to temperature and viscosity at four selected operating points. From left to right: (1 kHz, 5 mT), (1 kHz, 25 mT), (7 kHz, 5 mT), (6 kHz, 22.5 mT). (a) $\hat{\tau}$ versus temperature at four different viscosity levels, and (b) $\hat{\tau}$ versus viscosity at five different temperatures. Here, each dot represents a measurement (all three repetitions marked separately), and the lines correspond to the linear fits to $\hat{\tau}$ versus temperature or $\hat{\tau}$ versus viscosity. This procedure is repeated at all operating points, and the sensitivity metrics are computed using the slopes of the linear fits

(a) **Temperature sensitivity**

(b) **Viscosity sensitivity**

FIGURE 6 The estimated temperature and viscosity sensitivities at all operating points displayed as color maps. (a) The temperature sensitivities (in %/°C) at four different viscosity levels change relatively slowly across different operating points. (b) The viscosity sensitivities (in %/(mPa·s)) at five different temperatures show a drastic change as a function of drive field frequency, reaching the highest values of 10%/(mPa·s) at low frequencies around 1 kHz

0.36%/(mPa·s) at 25°C. Next, in Figure 6, the estimated sensitivities for temperature and viscosity for all operating points are given as color maps. Figure 6a shows temperature sensitivities at different operating points in units of %/°C, computed using Equation (10). Here, each subplot displays the temperature sensitivities at distinct viscosity levels from 0.9 mPa·s to 3.6 mPa·s. As seen in these results, temperature sensitivity changes relatively slowly across different operating points, displaying a smooth trend. The highest temperature sensitivity of 1.18 %/°C is achieved at (1 kHz, 5 mT) at 1.8 mPa·s. As a function of viscosity, temperature sensitivities have the highest values at the lowest viscosity level of 0.9 mPa·s, and they fall down gradually at higher viscosity levels.

The viscosity sensitivities at different operating points estimated using Equation (11) are shown in Figure 6b, in units of %/(mPa·s). Here, each subplot corresponds to viscosity sensitivities at a distinct temperature from 25°C to 45°C. In contrast to the slowly varying changes seen in the temperature sensitivity maps, viscosity sensitivity displays a drastic change as a function of drive field frequency. As seen in this figure, viscosity sensitivity reaches values 10%/(mPa·s) at low frequencies around 1 kHz with a maximum value of 13.4%/(mPa·s) achieved at (1 kHz, 5 mT) at 30°C, but rapidly falls after 3 kHz. When evaluated as a function of temperature, viscos-
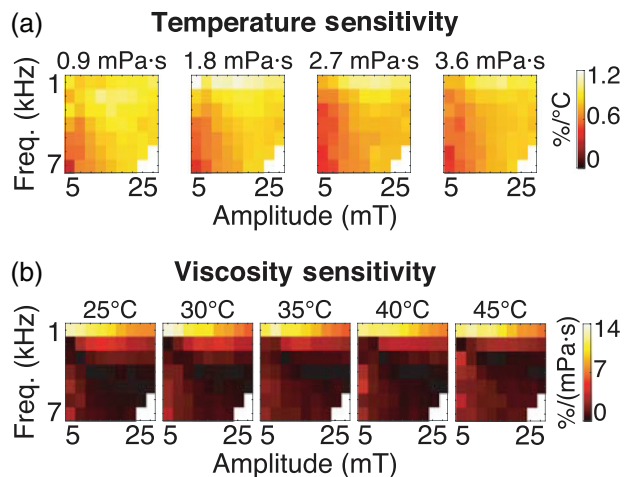
ity sensitivity remains almost constant showing relatively small variations at different temperatures.

Overall, Figure 6 clearly demonstrates viscosity-dependent temperature sensitivity and temperature-dependent viscosity sensitivity, underscoring the confounding effects of these two environmental parameters on the relaxation time constant.

5 | DISCUSSION

In this work, we analyzed the simultaneous effects of temperature and viscosity on relaxation time constant estimation via TAURUS. The results show that the drive field settings have a substantial impact on how sensitively τ responds to these environmental parameters. According to the results in Figure 6a, temperature sensitivity varies smoothly as a function of frequency and amplitude. In contrast, Figure 6b demonstrates that viscosity sensitivity is high at low frequencies around 1 kHz, whereas the time constants largely get desensitized to the viscosity effect for frequencies higher than 3 kHz. This result suggests that the Néel relaxation process, which does not depend on viscosity, may be the dominant mechanism at higher frequencies. Note that these results are in line with the previous work, which has shown that the Brownian relaxation is dominant at lower frequencies, whereas the Néel relaxation dominates at higher frequencies.[3,46–50] Based on these results, two different strategies can be envisioned for simultaneous temperature and viscosity estimation via TAURUS: (1) Performing measurements at two different drive field frequencies, for example, one measurement at (1 kHz,

5 mT) where both temperature and viscosity sensitivities are high, and another measurement at (4 kHz, 15 mT) where viscosity sensitivity is minimized but temperature sensitivity is still high. (2) Performing measurements at two different drive field amplitudes at a fixed frequency around 1 kHz, for example, one measurement at (1 kHz, 5 mT) where both temperature and viscosity sensitivities are high, and another measurement at (1 kHz, 25 mT) where temperature sensitivity is high but viscosity sensitivity is considerably lower. Alternatively, if the goal is to estimate the temperature alone, a single measurement can be performed at a medium-to-high amplitude drive field at frequencies above 3 kHz, where the signal is largely desensitized to the viscosity effect but is highly sensitive to temperature.

The temperature and viscosity metrics in Equations (10) (11) were defined using the slopes of the linear fits to $\hat{\tau}$ versus temperature and $\hat{\tau}$ versus viscosity curves. According to Equations (5) (6), while τ_B linearly depends on viscosity, neither τ_B nor τ_N has linear dependence with respect to temperature. However, from 25°C to 45°C, the absolute temperature in Kelvin changes by only about 6.7%. In this narrow range of temperatures, a linear approximation to $\hat{\tau}$ versus temperature shows a very good fit with the measurements, as seen in Figure 5a. Despite the small change in absolute temperature, the estimated time constants change by more than 20% at the highest sensitivity operating points, underscoring the temperature estimation capability of TAURUS. For the operating points tested in this work, the highest temperature sensitivity of TAURUS reaches 1.18%/°C. As a comparison, MRI thermometry was shown to have the following sensitivity levels[51]: equilibrium magnetization M_0 has a sensitivity of 0.3%/°C, T_1 relaxation constant has a sensitivity of 1%/°C, and the resonance frequency has a sensitivity of 0.01 ppm/°C. While some of these sensitivities are comparable to that of TAURUS, MFH treatments cannot be integrated within an MRI scanner, as the static B_0 field would saturate the MNP response. In contrast, MPI is compatible with MFH and provides localized heating capability, all the while promising high sensitivity thermometry. It should be noted that for in vivo cases, the accuracy of τ estimation itself will be as important as temperature sensitivity in determining the performance of MPI thermometry.

In contrast to the relatively small 6.7% change in absolute temperature, the change in viscosity from 0.9 to 3.6 mPa·s is fourfold. While Equation (5) indicates a linear relationship between τ_B and viscosity for the zero-field case, τ as measured in this work is an effective relaxation time constant that does not correspond to either the Brownian or the Néel relaxations alone and the zero-field assumption does not apply for AC fields. Consequently, in this wide range of viscosity levels, the linear fits to $\hat{\tau}$ versus viscosity curves may not reflect the true trends. For example, in Figure 5b, $\hat{\tau}$ shows a nonlinear trend especially at (1 kHz, 5 mT). The highest viscosity sensitivity of 13.4%/(mPa·s) is also achieved at this operating point. If the linear fits were computed using the lowest two viscosity levels of 0.9–1.8 mPa·s, the viscosity sensitivity would reach even higher values of 30%/(mPa·s) at 1 kHz. These high viscosity sensitivities underline the cancer imaging potential of MPI via viscosity mapping, as tumor microenvironment is known to have high-viscosity levels.[52]

According to Figure 6, temperature sensitivity decreases with viscosity. As given in Equations (5) and (6), viscosity is only effective on the Brownian relaxation process, whereas temperature is effective on both the Néel and Brownian relaxations. At higher viscosity levels, the relaxation starts to get dominated by the Néel relaxation, as the Brownian rotation significantly slows down.[53,54] Consequently, temperature sensitivity may be higher at low viscosity levels as it has both Brownian and Néel contributions, while being restricted to the Néel contribution alone at higher viscosity levels, explaining the decrease in temperature sensitivity.

The experiments in this work were performed in an arbitrary waveform MPS setup that enabled us to rapidly cover a wide range of operating points. It is important to note that TAURUS can be directly applied to MPI imaging experiments as well.[9,30] With that said, our previous work has shown that τ versus viscosity curves follow similar trends for both MPS and MPI cases, but with a given trend observed at higher frequencies for the MPI case.[9] Furthermore, our previous MPS results have demonstrated that τ versus viscosity curves of different MNPs also showed similar trends but at different frequencies.[6] Both of these observations indicate that there are underlying global trends in τ dictated by MNP characteristics and environmental conditions, and that MPS results can be utilized to forecast MPI results. Notwithstanding, a similar analysis to the one presented in this work should also be performed to demonstrate the simultaneous temperature and viscosity mapping capability of relaxation-based color MPI for imaging applications and using different MNPs, which remains an important future work.

6 | CONCLUSION

In this work, highly promising temperature sensitivity and viscosity sensitivity levels were demonstrated for relaxation time constant estimation via TAURUS, underlining its capability for simultaneous estimation of these environmental parameters. The results of the extensive experiments performed on our in-house arbitrary waveform MPS setup show that the temperature sensitivity changes slowly across different drive field settings, while the viscosity sensitivity is high at low frequencies around 1 kHz and rapidly falls after 3 kHz. These results

suggest that simultaneous estimation of temperature and viscosity can be achieved by performing measurements at two different drive field settings with complementary temperature/viscosity sensitivities. Alternatively, temperature estimation alone can be achieved at frequencies above 3 kHz by desensitizing the signal to the viscosity effect. The presented results also highlight the promise of MPI for functional imaging, and the potential of a hybrid MPI–MFH system for real-time monitored and localized thermal ablation treatment of cancer.

CONFLICT OF INTEREST
The authors have no conflicts to disclose.

DATA AVAILABILITY STATEMENT
The data that support the findings of this study are available from the corresponding author upon reasonable request.

REFERENCES

1. Gleich B, Weizenecker J. Tomographic imaging using the nonlinear response of magnetic particles. *Nature*. 2005;435:1214-1217.
2. Saritas EU, Goodwill PW, Croft LR, et al. Magnetic particle imaging (MPI) for NMR and MRI researchers. *J Magn Reson*. 2013;229:116-126.
3. Weaver JB, Rauwerdink AM, Hansen EW. Magnetic nanoparticle temperature estimation. *Med Phys*. 2009;36:1822-1829.
4. Stehning C, Gleich B, , , Gleich BRahmer J. Simultaneous magnetic particle imaging (MPI) and temperature mapping using multi-color MPI. *Int J Magn Part Imaging*. 2016;2:1-6.
5. Zhong J, Schilling M, Ludwig F. Magnetic nanoparticle temperature imaging with a scanning magnetic particle spectrometer. *Meas Sci Technol*. 2018;29:115903.
6. Utkur M, Muslu Y, Saritas EU. Relaxation-based viscosity mapping for magnetic particle imaging. *Phys Med Biol*. 2017;62:3422-3439.
7. Shasha C, Teeman E, Krishnan KM. Harmonic simulation study of simultaneous nanoparticle size and viscosity differentiation. *IEEE Magn Lett*. 2017;8:1-5.
8. Möddel M, Meins C, Dieckhoff J, Knopp T. Viscosity quantification using multi-contrast magnetic particle imaging. *New J Phys*. 2018;20:083001.
9. Utkur M, Muslu Y, Saritas E. Relaxation-based color magnetic particle imaging for viscosity mapping. *Appl Phys Lett*. 2019;115.
10. Weaver JB, Ness DB, Fields J, et al. Identifying in vivo inflammation using magnetic nanoparticle spectra. *Phys Med Biol*. 2020;65:125003.
11. Chandrasekharan P, Fung KB, Zhou XY, et al. Non-radioactive and sensitive tracking of neutrophils towards inflammation using antibody functionalized magnetic particle imaging tracers. *Nanotheranostics*. 2021;5:240-255.
12. Yu EY, Bishop M, Zheng B, et al. Magnetic particle imaging: a novel in vivo imaging platform for cancer detection. *Nano Lett*. 2017;17:1648-1654.
13. Wells J, Löwa N, Paysen H, Steinhoff U, Wiekhorst F. Probing particle-matrix interactions during magnetic particle spectroscopy. *J Magn Magn Mater*. 2019;475:421-428.
14. Rivera-Rodriguez A, Hoang-Minh LB, et al. Tracking adoptive T cell immunotherapy using magnetic particle imaging. *Nanotheranostics*. 2021;5(4):431–444. https://doi.org/10.7150/ntno.55165
15. Ohki A, Kuboyabu T, Aoki M, Yamawaki M, Murase K. Quantitative evaluation of tumor response to combination of magnetic hyperthermia treatment and radiation therapy using magnetic particle imaging. *Int Nanomed and Nanosurg*. 2016;2(3). https://doi.org/10.16966/2470-3206.117
16. Tay ZW, Chandrasekharan P, Chiu-Lam A, et al. Magnetic particle imaging-guided heating in vivo using gradient fields for arbitrary localization of magnetic hyperthermia therapy. *ACS Nano*. 2018;12:3699-3713.
17. Wells J, Twamley S, Sekar A, Ludwig A, Paysen H, Kosch O, Wiekhorst F. Lissajous scanning magnetic particle imaging as a multifunctional platform for magnetic hyperthermia therapy. *Nanoscale*. 2020;12:18342-18355.
18. Hensley D, Tay ZW, Dhavalikar R, et al. Combining magnetic particle imaging and magnetic fluid hyperthermia in a theranostic platform. *Phys Med Biol*. 2017;62:3483-3500.
19. Myrovali E, Maniotis N, Samaras T, Angelakeris M. Spatial focusing of magnetic particle hyperthermia. *Nanoscale Adv*. 2020;2:408-416.
20. Murase K, Aoki M, Banura N, et al. Usefulness of Magnetic particle imaging for predicting the therapeutic effect of magnetic hyperthermia. *Open J Med Imaging*. 2015;05:85-99.
21. Wells J, Paysen H, Kosch O, Trahms L, Wiekhorst F. Temperature dependence in magnetic particle imaging. *AIP Adv*. 2018;8:056703.
22. Chapelon JY, Ribault M, Birer A, Vernier F, Souchon R, Gelet A. Treatment of localised prostate cancer with transrectal high intensity focused ultrasound. *Eur J Ultrasound*. 1999;9:31-38.
23. Huber PE, Jenne JW, Rastert R, et al. A new noninvasive approach in breast cancer therapy using magnetic resonance imaging-guided focused ultrasound surgery. *Cancer Res*. 2001;61:8441-8447.
24. Salomir R, Delemazure A-S, Palussière J, Rouvière O, Cotton F, Chapelon J-Y. Image-based control of the magnetic resonance imaging-guided focused ultrasound thermotherapy. *Top Magn Reson Imaging*. 2006;17:139-151.
25. Rauwerdink AM, Hansen EW, Weaver JB. Nanoparticle temperature estimation in combined AC and DC magnetic fields. *Phys Med Biol*. 2009;54:51.
26. Perreard IM, Reeves DB, Zhang X, Kuehlert E, Forauer ER, Weaver JB. Temperature of the magnetic nanoparticle microenvironment: estimation from relaxation times. *Phys Med Biol*. 2014;59:1109-1119.
27. Zhong J, Schilling M, Ludwig F. Excitation frequency dependence of temperature resolution in magnetic nanoparticle temperature imaging with a scanning magnetic particle spectrometer. *J Magn Magn Mater*. 2019;471:340-345.
28. Salamon J, Dieckhoff J, Kaul MG, et al. Visualization of spatial and temporal temperature distributions with magnetic particle imaging for liver tumor ablation therapy. *Sci Rep*. 2020;10:7480.
29. Draack S, Schilling M, Viereck T. Magnetic particle imaging of particle dynamics in complex matrix systems. Odenbach S, *Magnetic Hybrid-Materials*. Germany: De Gruyter; 2021;297–321. https://doi.org/10.1515/9783110569636.
30. Muslu Y, Utkur M, Demirel OB, Saritas EU. Calibration-Free relaxation-based multi-color magnetic particle imaging. *IEEE Trans Med Imaging*. 2018;37:1920-1931.

31. Utkur M, Muslu Y & Saritas EU Confounding effects of temperature and viscosity towards relaxation mapping. In: 9th International Workshop on Magnetic Particle Imaging (IWMPI), New York. Infinite Science 2019: 223–224.

32. Zhang X. A surface wave elastography technique for measuring tissue viscoelastic properties. *Med Eng Phys*. 2017;42:111-115.

33. Goodwill PW, Conolly SM. The X-space formulation of the magnetic particle imaging process: 1-D signal, resolution, bandwidth, SNR, SAR, and magnetostimulation. *IEEE Trans Med Imaging*. 2010;29:1851-1859.

34. Knopp T, Buzug TM. . *Magnetic Particle Imaging*. : Springer-Verlag; 2012.

35. Neel L. Théorie du traînage magnétique des ferromagnétiques en grains fins avec application aux terres cuites. *Ann Géophys*. 1949;5:99-136.

36. Brown WF. Thermal fluctuations of a single-domain particle. *Phys Rev*. 1963;130:1677-1686.

37. Rosensweig RE. Heating magnetic fluid with alternating magnetic field. *J Magn Magn Mater*. 2002;252:370-374.

38. Shasha C, Krishnan KM. Nonequilibrium dynamics of magnetic nanoparticles with applications in biomedicine. *Adv Mater*. 2020;1904131.

39. Croft LR, Goodwill PW, Conolly SM. Relaxation in X-space magnetic particle imaging. *IEEE Trans Med Imaging*. 2012;31:2335-2342.

40. Croft LR, Goodwill PW, Konkle JJ, et al. Low drive field amplitude for improved image resolution in magnetic particle imaging. *Med Phys*. 2015;43:424-435.

41. Cheng N-S. Formula for the viscosity of a glycerol-water mixture. *Ind Eng Chem Res*. 2008;47:3285-3288.

42. Physical Properties of glycerine and its solutions (Technical report). Glycerine Producers' Association; 1963.

43. Fierro P, Nyer EK, editors. *The Water Encyclopedia: Hydrologic Data and Internet Resources*. CRC/Taylor and Francis; 2007.

44. Tay ZW, Goodwill PW, Hensley DW, Taylor LA, Zheng B, Conolly SM. A high-throughput, arbitrary-waveform, MPI spectrometer and relaxometer for comprehensive magnetic particle optimization and characterization. *Sci Rep*. 2016;6:34180.

45. Top CB. An arbitrary waveform magnetic nanoparticle relaxometer with an asymmetrical three-section gradiometric receive coil. *Turk J Electr Eng Comput Sci*. 2020;28:1344-1354.

46. Wawrzik T, Ludwig F, Schilling M. Magnetic particle imaging: Exploring particle mobility. In: Buzug TM, Borgert J, eds. *Magnetic Particle Imaging: A Novel SPIO Nanoparticle Imaging Technique*. Springer; 2012: 21-25.

47. Dieckhoff J, Eberbeck D, Schilling M, Ludwig F. Magnetic-field dependence of Brownian and Néel relaxation times. *J Appl Phys*. 2016;119:043903.

48. Ota S, Kitaguchi R, Takeda R, Yamada T, Takemura Y. Rotation of magnetization derived from Brownian relaxation in magnetic fluids of different viscosity evaluated by dynamic hysteresis measurements over a wide frequency range. *Nanomaterials*. 2016;6:170.

49. Viereck T, Kuhlmann C, Draack S, Schilling M, Ludwig F. Dual-frequency magnetic particle imaging of the Brownian particle contribution. *J Magn Magn Mater*. 2017;427:156-161.

50. Yoshida T, Nakamura T, Higashi O, Enpuku K. Effect of viscosity on the AC magnetization of magnetic nanoparticles under different AC excitation fields. *J Magn Magn Mater*. 2019;471:334-339.

51. Rieke V, Butts Pauly K. MR thermometry. *J Magn Reson Imaging*. 2008;27:376-390.

52. Yin J, Kong X, Lin W. Noninvasive cancer diagnosis in vivo based on a viscosity-activated near-infrared fluorescent probe. *Anal Chem*. 2021;93:2072-2081.

53. Wiedenmann A, Gähler R, Dewhurst CD, Keiderling U, Prévost S, Kohlbrecher J. Relaxation mechanisms in magnetic colloids studied by stroboscopic spin-polarized small-angle neutron scattering. *Phys Rev B*. 2011;84:214303.

54. Andrade ÂL, Cavalcante LCD, Fabris JD, et al. Magnetically induced heating by iron oxide nanoparticles dispersed in liquids of different viscosities. *Ceram Int*. 2020;46:21496-21504.